IEEE Access
Multidisciplinary | Rapid Review | Open Access Journal

Received April 1, 2021, accepted April 9, 2021, date of publication April 12, 2021, date of current version April 20, 2021.

Digital Object Identifier 10.1109/ACCESS.2021.3072672

A Rotary-Linear SPM Voice Coil Motor With PM Flux Bridges for Output Performance Improvement

FUZHEN XING, JUNG-WOO KWON, MINGJIE LI, AND BYUNG-IL KWON, (Senior Member, IEEE)
Department of Electrical Systems Engineering, Hanyang University, Ansan 15588, South Korea

Corresponding author: Byung-Il Kwon (bikwon@hanyang.ac.kr)

This work was supported in part by the National Research Foundation of Korea Grant funded by the Korean Government Ministry of Science under Grant NRF-2020R1A2B5B01002400, and in part by the National Research Foundation of Korea within the Ministry of Education through the BK21FOUR Program.

ABSTRACT This paper proposes a rotary-linear surface-mounted permanent magnet (PM) voice coil motor (RL-SVCM) with PM flux bridges in place of the iron flux bridges in a traditional RL-SVCM for enhancing average torque and force ripple but slight damage of torque ripple and average linear force. The iron flux bridges in a basic RL-SVCM cannot participate in the generation of rotary torque. In contrast, the PM flux bridges in the proposed RL-SVCM can participate in the generation of rotary torque. The magnetic equivalent circuit (MEC) is used to analyze the magnetic circuits of the basic and proposed models. The results explain the reasons for the performance improvements achieved by the proposed motor. The finite element method (FEM) is used to derive the precise output performance of the basic and proposed motors. Additionally, a prototype of the proposed RL-SVCM with PM flux bridges was manufactured for experimental verification. Close agreement between the experimental results and FEM results validates the feasibility of the proposed RL-SVCM.

INDEX TERMS Rotary-linear motor, two-degree-of-freedom motion, voice coil motor (VCM).

I. INTRODUCTION

Recently, the demand for compact, lightweight, and high-performance rotary-linear (RL) motion modules [1]–[3] has increased significantly in the manufacturing industries for semiconductor packaging, medicine, and aviation. However, a traditional RL motion module requires two sets of rotary motors and a mechanical transmission. Motion accuracy and responses are limited by mechanical transmission errors, meaning traditional RL motion modules must be replaced with high-precision, direct-drive, and compact RL motors.

According to the different structures of magnetic flux circuit fields, two-degree-of-freedom (2DoF) RL motors can be divided into two main categories. One category is 2DoF motors with crossed RL magnetic fields. Many studies have investigated this type of system, including studies on helical-winding 2DoF motors [4], [5], salient-pole 2DoF motors [6], [7], and double-stator 2DoF motors [8]–[10]. In reference [11], [12], high-temperature superconducting field windings are imbedded in the stator to achieve the linear motion, but special working conditions are needed. Moreover, these types of motors have the same characteristics as highly integrated complex motors and strong coupling effects. The second category is 2DoF motors with an independent RL magnetic field. There have also been many studies on this type of motor, including studies on multi-stator 2DoF motors [13] and voice-coil-structure 2DoF motors [14], [15]. These types of motors have the same characteristics as low-coupling-effect motors, but the integration level is low, as shown in Table 1. The common disadvantages of the existed voice-coil-structures are complex motor structure, low torque density, and difficult speed control system.

Therefore, to develop an RL motor with low coupling effects and strong integration, an RL motor with a surface-mounted permanent magnet (SPM) and voice coil (RL-SVCM) structure was developed in [16], as shown in Figure 1. The RL-SVCM has a relatively simple structure, the output ripples of torque and force are small, and

The associate editor coordinating the review of this manuscript and approving it for publication was Jinquan Xu.

TABLE 1. Qualitative comparison of the 2DoF RL motors.

Items	Motors with crossed RL magnetic fields	Motors with independent RL magnetic fields
Coupling effect	High	Low
Integration level	High	Low

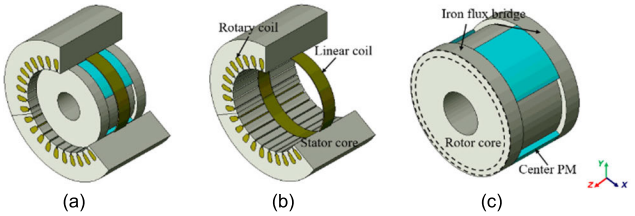

FIGURE 1. The basic model of an RL-SVCM with iron flux bridges: (a) machine topology, (b) stator, and (c) rotor.

the PM bridges in the proposed model can work for both rotary and linear motion simultaneously, which significantly improves the utilization of the PM. In contrast, in a traditional RL-SVCM with iron flux bridges, the iron flux bridges at the end of the rotor only participate in the generation of the linear force and cannot participate in the generation of rotational torque. Therefore, iron flux bridges are not fully utilized, which means the low power density.

This paper proposes an RL-SVCM with PM flux bridges for output performance improvement. The PM flux bridges in the proposed model contribute to rotational torque generation, unlike the iron flux bridges in the basic model. The magnetic equivalent circuit (MEC) method theoretically explains why the performance of the proposed model is improved compared to the basic model. The finite element method (FEM) is used to analyze the precise output performance of the basic and proposed models. A prototype of the proposed RL-SVCM with PM flux bridges was manufactured for experimental verification. Strong agreement between the experimental results and FEM results proves the feasibility of the proposed RL-SVCM.

II. MACHINE TOPOLOGY

A. BASIC MODEL OF AN RL-SVCM WITH IRON FLUX BRIDGES

A basic RL-SVCM with iron flux bridges [16] is presented in Figure 1(a). The stator contains two control circuits, as shown in Figure 1(b). One is a rotary coil with five phases [17]–[22] inserted in the stator slot. The other is a voice coil, which is defined as a linear coil. Each coil is labelled in Figure 1(b).

The basic model has a rotor equipped with three center PMs. The center PMs in the basic model contribute to both rotary torque and linear force as a magnetic flux source. At each end of the rotor, ring-type iron flux bridges encase the rotor. They are distinguished from the rotor body by the dotted lines in Figure 1(c). Iron flux bridges contribute to linear motion by guiding the flow of magnetic flux from the rotor to the stator.

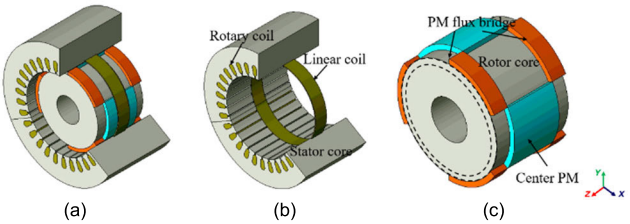

FIGURE 2. Proposed model of an RL-SVCM with PM flux bridges: (a) machine topology, (b) stator, and (c) rotor.

TABLE 2. Parameters of the basic and proposed RL-SVCMs.

Item	Unit	Value
Stator slots	-	30
Magnet poles	-	3
Stator axial length	mm	110
Rotor axial length	mm	80
Stator in/outside diameter	mm	119.4/170
Linear coil in/outside diameter	mm	117.4/119.4
Rotor in/outside diameter	mm	96/116
Linear motion active moving length	mm	30
Center PM length	mm	50
PM material	-	Nd-Fe-B
PM flux bridge radian (each)	°	60
Rotary coil turns (each slot)	n	170
Linear coil turns	n	20
Air gap length	mm	0.7
Rated speed	RPM	1800

B. PROPOSED MODEL FOR AN RL-SVCM WITH PM FLUX BRIDGES

We propose an RL-SVCM with PM flux bridges instead of iron flux bridges for improved torque density.

The proposed model RL-SVCM with PM flux bridges is illustrated in Figure 2(a). The stator of the proposed model has same structure as that of the basic model, as shown in Figure 2(b). The rotor not only has three center PMs, but also has an additional three PMs acting as PM flux bridges at each end, as shown in Figure 2(c).

These PM flux bridges take on the role of the iron flux bridges in the basic model. The replacement of iron flux bridges with PM flux bridges is indicated by dotted lines for ease of visualization. These PM flux bridges have opposite magnetization directions compared to the center PMs. The PM flux bridges and center PMs have the same pole arc angle and are positioned in intervals of one pole arc, as shown in Figure 2(c).

The parameters for the basic model and proposed model are listed in Table 2.

III. MEC ANALYSIS

To prove the performance improvements of the proposed model compared to the basic model theoretically, MEC analysis was performed. MEC analysis utilizes partitioned modeling for the simplification of calculation.

A. MEC ANALYSIS OF ROTARY MOTION

MEC analysis can be performed easily on two-dimensional models of machines with symmetrical structures about the z axis. However, the basic RL-SVCM has asymmetrical

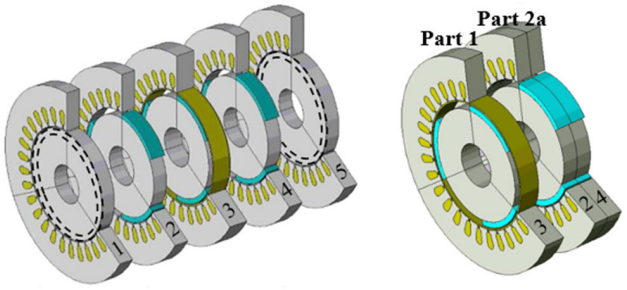

FIGURE 3. Basic model of an RL-SVCM: (a) separation model and (b) equivalent model.

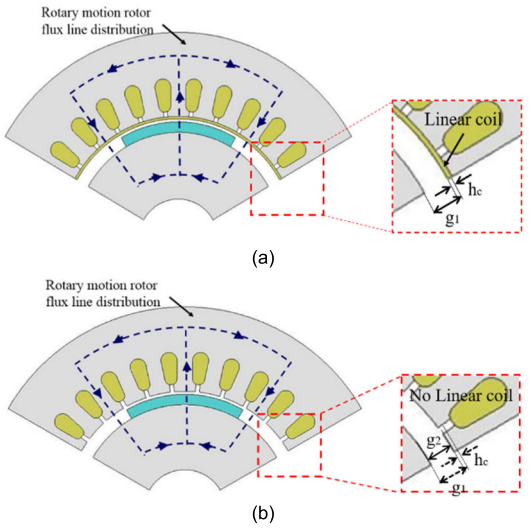

FIGURE 4. Basic model of an RL-SVCM rotary motion flux line distribution: (a) part 1 and (b) part 2a.

structures about the z axis, as shown in Figure 3(a). Therefore, to discriminate different structures, the basic model is first divided into five partitions labeled with numbers of 1 to 5, as shown in Figure 3(b).

The torque of a PM motor consists of PM torque and reluctance torque. In Figure 3(b), there are two partitions with labels of 1 and 5 containing the iron flux bridges. In these partitions, there are no PMs, meaning no PM torque can be generated. Additionally, the structure has no saliency, meaning no reluctance torque can be generated.

Therefore, partitions 1 and 5, which contain the iron flux bridges of the basic model, do not contribute to rotary torque generation [23]. Therefore, partitions 1 and 5 of the basic model can be ignored for rotary torque calculation.

To simplify the calculation of torque production for the remaining partitions 2, 3, and 4, they are arranged as shown in Figure 3(b). The sub-assemblies are labeled as part 1 and part 2a.

The flux line distribution of part 1 in Figure 3(b) is presented in Figure 4(a). The flux line distribution of part 2a in Figure 3(b) is presented in Figure 4(b). Because the linear coil is embedded in the stator for part 1, the air gap differs between parts 1 and 2. The air gap in part 1, denoted as g_1,

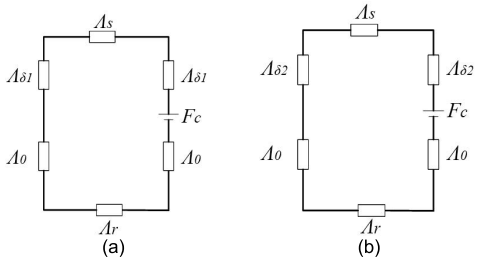

FIGURE 5. MECs for basic model rotary motion: (a) part 1 and (b) part 2a.

includes the length of the linear coil h_c, making it larger than the air gap in part 2a, denoted as g_2.

MECs for parts 1 and 2a are presented in Figure 5(a) and 5(b), respectively. Here, Λ_s and Λ_r are the steel sheet permeance of the stator and rotor, respectively. $\Lambda_{\delta 1}$ is the air gap permeance in part 1, $\Lambda_{\delta 2}$ is the air gap permeance in part 2a, and Λ_0 is the PM permeance.

Because the air gap in part 1 is larger than that in part 2a, $1 / \Lambda_{\delta 1}$ is greater than $1 / \Lambda_{\delta 2}$. The air gap fluxes of basic model part 1 ϕ_{Fp1} and part 2a ϕ_{Fp2} can be calculated as follows:

$$\begin{cases} \varphi_{Fp1} = \dfrac{F_c}{2/\Lambda_{\delta 1} + 2/\Lambda_0 + 1/\Lambda_s + 1/\Lambda_r} \\ \qquad \approx \dfrac{F_c}{2/\Lambda_{\delta 1} + 2/\Lambda_0} \\ \varphi_{Fp2} = \dfrac{F_c}{2/\Lambda_{\delta 2} + 2/\Lambda_0 + 1/\Lambda_s + 1/\Lambda_r} \\ \qquad \approx \dfrac{F_c}{2/\Lambda_{\delta 2} + 2/\Lambda_0}. \end{cases} \tag{1}$$

Therefore, the average torque of the basic model can be calculated as follows:

$$\begin{aligned} T_{\text{Bave}} &= \frac{3EI}{2\omega r} \\ &= 3IRNk_{\omega 1}(B_{Fp1}L_{Fp1} + B_{Fp2}L_{Fp2}) \\ &= 3IRNk_{\omega 1}\left(\frac{\varphi_{Fp1}}{A_{Fp1}}L_{Fp1} + \frac{\varphi_{Fp2}}{A_{Fp2}}L_{Fp2}\right) \\ &= T_1 + T_2 \\ &\quad \left(T_1 = 3IRNk_{\omega 1}\frac{\varphi_{Fp1}}{A_{Fp1}}L_{Fp1},\ T_2 = 3IRNk_{\omega 1}\frac{\varphi_{Fp2}}{A_{Fp2}}L_{Fp2}\right), \end{aligned} \tag{2}$$

where L_{Fp1} is the z-axis length of part 1 in Figure 3(b) and L_{Fp2} is the z-axis length of part 2a in Figure 3(b). T_1 and T_2 represent the torque generated by parts 1 and 2a, respectively.

The proposed RL-SVCM also has asymmetrical structures about the z axis, as shown in Figure 6(a).

Therefore, to discriminate different structures, the proposed model is also divided into five partitions and labeled with numbers from 1 to 5, as shown in Figure 6(b). The difference between the proposed and basic models is that the proposed model has PM flux bridges in partitions 1 and 5. Similar to the basic model, the divided partitions are assembled as shown in Figure 6(b) to simplify the calculation of torque production. Here, the sub-assemblies are labeled as parts 1 and 2b.

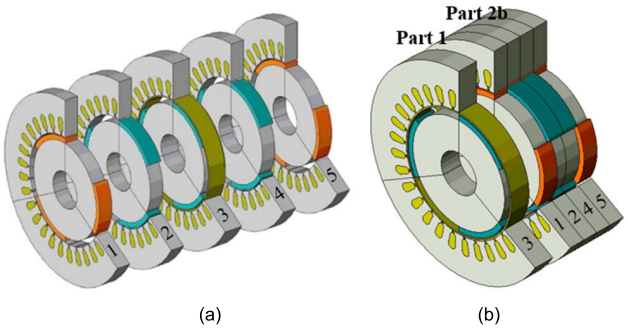

FIGURE 6. Proposed model for an RL-SVCM: (a) separation model and (b) equivalent model.

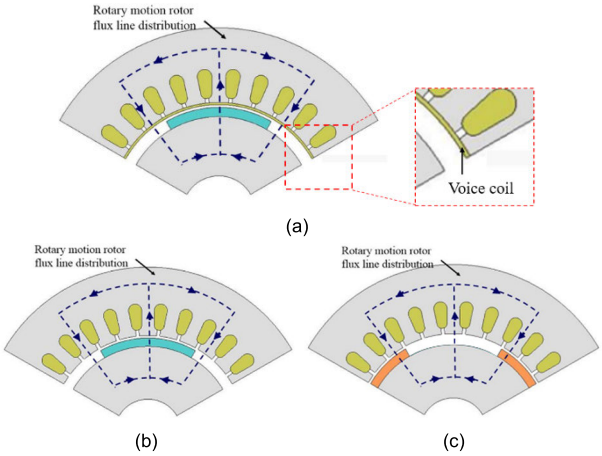

FIGURE 7. Proposed model for an RL-SVCM: rotary motion flux line distributions in (a) part 1, (b) part 2b partitions 2 and 4, and (c) part 2b partitions 1 and 5.

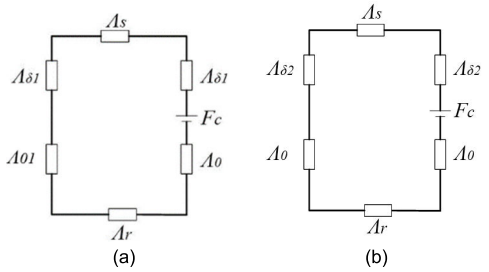

FIGURE 8. MECs for the proposed rotary motor: (a) part 1 and (b) part 2b.

The flux line distribution in part 1 from Figure 6(b) is presented in Figure 7(a). The flux line distribution in part 2b is presented for two different pairs of partitions in Figures 7(b) and 7(c).

Just as in the basic model, the linear coil is embedded in the stator, meaning the air gap differs between parts 1 and 2. Unlike in the basic model, partitions 1 and 5 must be considered because they contribute to the rotary torque. Although the configurations of partitions 1 and 5 differ from those of partitions 2 and 4 based on different PM magnetization directions and PM arrangements, they have the same resultant flux line distribution. Therefore, they have the same air gap flux.

MECs for parts 1 and 2b are presented in Figures 8(a) and 8(b), respectively. Just as in the basic model, the air gap in part 1 is larger than that in part 2b, meaning $1 / \Lambda_{\delta 1}$ is greater than $1 / \Lambda_{\delta 2}$.

The fluxes of the proposed model part 1 ϕ_{Pp1} and part 2b ϕ_{Pp2} can be calculated as follows:

$$\begin{cases} \varphi_{Pp1} = \dfrac{F_c}{2/\Lambda_{\delta 1} + 2/\Lambda_0 + 1/\Lambda_s + 1/\Lambda_r} \\ \quad \approx \dfrac{F_c}{2/\Lambda_{\delta 1} + 2/\Lambda_0} \\ \varphi_{Pp2} = \dfrac{F_c}{2/\Lambda_{\delta 2} + 2/\Lambda_0 + 1/\Lambda_s + 1/\Lambda_r} \\ \quad \approx \dfrac{F_c}{2/\Lambda_{\delta 2} + 2/\Lambda_0} \end{cases} \tag{3}$$

Therefore, the average torque of the proposed model can be calculated as follows:

$$\begin{aligned} T_{\text{Pave}} &= \frac{3EI}{2\omega r} \\ &= 3IRNk_{\omega 1}(B_{Pp1}L_{Pp1} + B_{Pp2}L_{Pp2}) \\ &= 3IRNk_{\omega 1}(\frac{\varphi_{Pp1}}{A_{Pp1}}L_{Pp1} + \frac{\varphi_{Pp2}}{A_{Pp2}}L_{Pp2}) \\ &= T_1 + 2T_2, \end{aligned} \tag{4}$$

where L_{Pp1} is the z-axis length of part 1 in Figure 6(b) and L_{Pp2} is the z-axis length of part 2b in Figure 6(b). ϕ_{Fp1}, ϕ_{Fp2}, and L_{Fp1} are the same as ϕ_{Pp1}, ϕ_{Pp2}, and L_{Pp1} in Equation (2), respectively. Unlike part 2a in the basic model, which contains two partitions, part 2b in the proposed motor contains four partitions, as shown in Figure 6(b). Additionally, the four partitions in part 2b are equivalent, as shown in Figure 7(b). Therefore, the torque generated by part 2b T_2' in the proposed model is two times of T_2, as shown in Equation (4).

When comparing Equations (2) and (4), it can be concluded that the average torque of the proposed model is greater than that of the basic model.

B. MEC ANALYSIS OF LINEAR MOTION

The operating principle of basic model linear motion [16] is the same as that in a conventional voice coil motor [24]–[31], as represented in 2D in Figure 9.

Based on Figure 9, an MEC is presented in Figure 10(a), where Λ_σ is the permeance of the leakage flux, Λ_0 is the permeance of the PM, Λ_{L1} and Λ_{L2} are the left parts of the stator and rotor axial steel sheet permeance values, respectively, Λ_{R1} and Λ_{R2} are the right parts of the stator and rotor axial steel sheet permeance values, respectively, and $\Lambda_{\delta 1}$ and $\Lambda_{\delta 2}$ are the permeance values of the linear air gaps.

To simplify the MEC in Figure 10(a), Equation (5) is applied.

$$\Lambda_L = \Lambda_{L1} // \Lambda_{L2} // \Lambda_{\delta 2} \tag{5-a}$$

$$\Lambda_R = \Lambda_{R1} // \Lambda_{R2} // \Lambda_{\delta 2} \tag{5-b}$$

In this manner, Figure 10(a) can be simplified to produce Figure 10(b). To simplify Figure 10(b), the structural permeance Λ can be defined as follows:

$$\Lambda = \Lambda_L + \Lambda_R, \tag{6-a}$$

$$\frac{1}{\Lambda} = \frac{1}{\Lambda_L} // \frac{1}{\Lambda_R}. \tag{6-b}$$

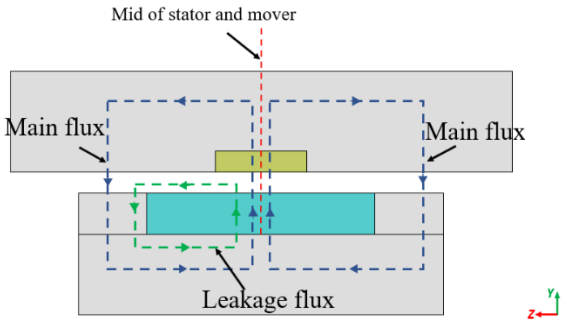

FIGURE 9. Basic model of an RL-SVCM with iron flux bridges under linear motion.

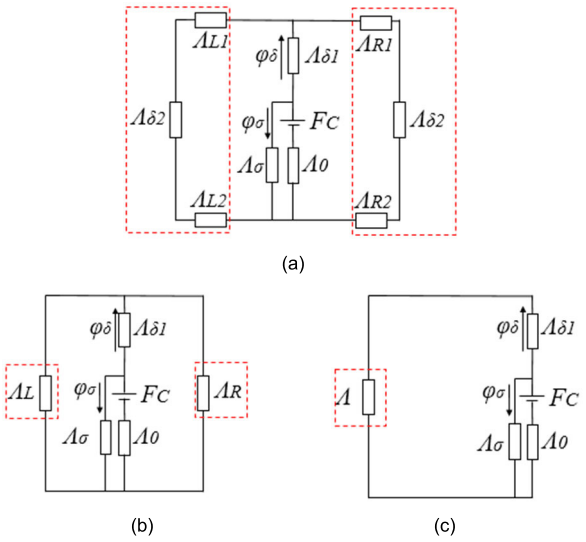

FIGURE 10. MECs for basic model linear motion: (a) Original MEC, (b) simplified MEC 1, and (c) simplified MEC 2.

In this manner, Figure 10(b) can be simplified to produce figure 10(c). Based on Figure 10(c), the magnetic flux φ_δ in the air gap can be calculated as follows:

$$\varphi_\delta = \frac{F_C \Lambda_o}{1 + (\Lambda_\sigma + \Lambda_o)(\frac{1}{\Lambda} + \frac{1}{\Lambda_{\delta 1}})}. \tag{7}$$

Additionally, the parameters in Equation (7) can be calculated as follows:

$$\begin{cases} F_c = H_c h_m \\ \Lambda_0 = \dfrac{\mu_r \mu_0 A_m}{h_m} \\ \Lambda_{\delta 1} = \dfrac{\mu_0 A_{\delta 1}}{\delta_1}, \end{cases} \tag{8}$$

where μ_0 is the permeability of a vacuum, μ_r is the relative magnetic permeability of the PMs, A_m is the cross-sectional area of the magnetic flux excited by the PMs, h_m is the magnetization length of the PM in the linear section, δ_l is the length of the mechanical air gaps over the voice coil, and H_C is the coercive force of the permanent magnet. Substituting Equation (8) into Equation (7) yields

$$\varphi_\delta = \frac{H_c \mu_r \mu_0 A_m}{1 + (\Lambda_\sigma + \frac{\mu_r \mu_0 A_m}{h_m})(\frac{1}{\Lambda} + \frac{\delta_1}{\mu_0 A_{\delta 1}})}. \tag{9}$$

A voice coil motor under linear motion follows the same principles as when current flows in the coil under a center magnetic field, meaning the coil experiences a force proportional to the inflow current [14]–[19]. Therefore, the linear force can be calculated as follows:

$$F_l = N_L B_\delta I_L L_r, \tag{10}$$

where B_δ is the magnetic flux density in the air gap of the linear section, N_L is the number of turns in the voice coil, I_L is the current in the conductors, and L_r is the average circumference of the coil. Additionally, B_δ can be expressed as follows:

$$B_\delta = \frac{\varphi_\delta}{A_m}. \tag{11}$$

Therefore, Equation (10) can be expressed as follows:

$$F_l = \frac{\varphi_\delta N_L I_L L_r}{A_m}. \tag{12}$$

By substituting Equation (9) into Equation (12), the linear force of the basic model F_l can be expressed as follows:

$$F_l = \frac{H_c \mu_r \mu_0 N_L I_L L_r}{1 + (\Lambda_\sigma + \frac{\mu_r \mu_0 A_m}{h_m})(\frac{1}{\Lambda} + \frac{\delta_1}{\mu_0 A_{\delta 1}})}. \tag{13}$$

According to (13), the linear force F_l will only be influenced by the equivalent structure permeance $1/\Lambda$ and the leakage flux permeance Λ_σ.

When the motor works with the linear coil and center PMs in line, as shown Figure 9, we have

$$\frac{1}{\Lambda_L} = \frac{1}{\Lambda_R}. \tag{14}$$

By combining (6-b) and (14), $1/\Lambda$ can be expressed as

$$\frac{1}{\Lambda} = \frac{1}{2\Lambda_L} = \frac{1}{2\Lambda_R}. \tag{15}$$

By ignoring the leakage flux permeance Λ_σ and substituting (15) into (13), we get the following linear force equation:

$$F_l = \frac{H_c \mu_r \mu_0 N_L I_L L_r}{1 + \frac{\mu_r \mu_0 A_m}{h_m}(\frac{1}{2\Lambda_L} + \frac{\delta_1}{\mu_0 A_{\delta 1}})}. \tag{16}$$

The proposed model under linear motion is also based on the operating principles of a voice coil motor, as shown in Figure 11. Based on Figure 11, an MEC is illustrated in Figure 12(a). Here, Λ_{01} is the permeance of the PM flux bridges, Λ_{FL1} and Λ_{FL2} are the permeance values of the left parts of the stator and rotor axial steel sheet, respectively, and Λ_{FR1} and Λ_{FR2} are permeance values of the right parts of the stator and rotor axial steel sheet, respectively.

To simplify the MEC in Figure 12(a), (17) is applied.

$$\Lambda_{FL} = \Lambda_{FL1} // \Lambda_{FL2} // \Lambda_{\delta 2} // \Lambda_{01} \tag{17-a}$$

$$\Lambda_{FR} = \Lambda_{FR1} // \Lambda_{FR2} // \Lambda_{\delta 2} // \Lambda_{01} \tag{17-b}$$

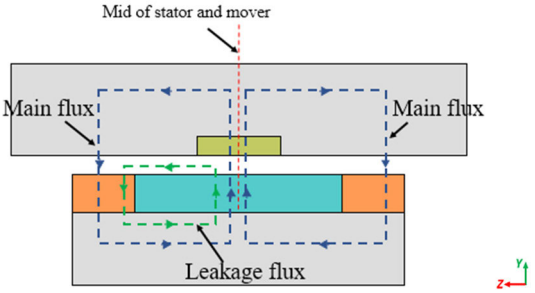

FIGURE 11. Proposed RL-SVCM 2D equivalent graph with PM flux bridges under linear motion.

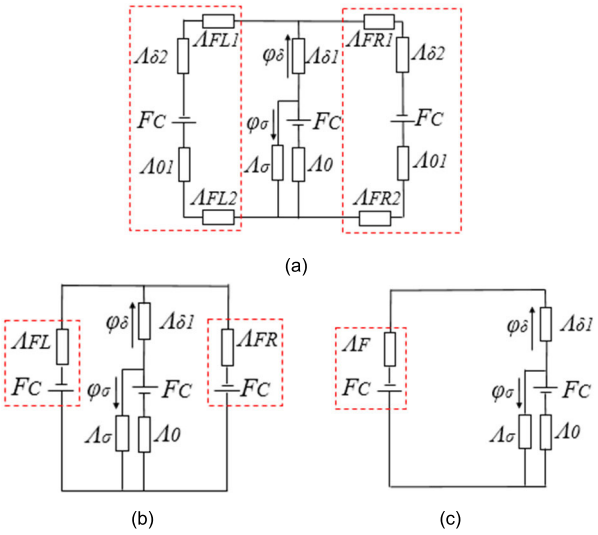

FIGURE 12. MEC for the proposed model under linear motion: (a) Original MEC; (b) simplified MEC 1, and (c) simplified MEC 2.

Therefore, Figure 12(a) can be simplified to produce Figure 12(b). Additionally, to simplify Figure 12(b), the structural permeance Λ_F can be defined as follows:

$$\Lambda_F = \Lambda_{FL} + \Lambda_{FR}, \tag{18-a}$$

$$\frac{1}{\Lambda_F} = \frac{1}{\Lambda_{FL}} // \frac{1}{\Lambda_{FR}}. \tag{18-b}$$

Therefore, Figure 12(b) can be simplified to produce Figure 12(c).

Based on Figure 12(c), the magnetic flux φ_δ in the air gap of the proposed model can be calculated as follows:

$$\varphi_\delta = \frac{2F_C\Lambda_o}{1 + (\Lambda_0 + \Lambda_\sigma)(\frac{1}{\Lambda_F} + \frac{1}{\Lambda_{\delta 1}})}. \tag{19}$$

Substituting (8) into (20) yields

$$\varphi_\delta = \frac{2H_c\mu_r\mu_0 A_m}{1 + (\frac{\mu_r\mu_0 A_m}{h_m} + \Lambda_\sigma)(\frac{1}{\Lambda_F} + \frac{\delta_1}{\mu_0 A_{\delta 1}})}. \tag{20}$$

By substituting (10), (11), and (12) into (20), the linear force F_{Fl} of the proposed model can be calculated as follows:

$$F_{Fl} = \frac{2H_c\mu_r\mu_0 N_L I_L L_r}{1 + (\frac{\mu_r\mu_0 A_m}{h_m} + \Lambda_\sigma)(\frac{1}{\Lambda_F} + \frac{\delta_1}{\mu_0 A_{\delta 1}})}. \tag{21}$$

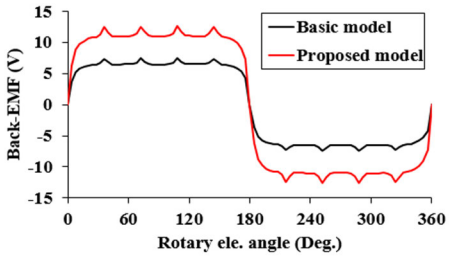

FIGURE 13. Back EMF of the rotary coils.

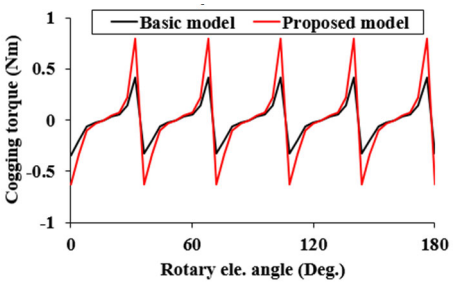

FIGURE 14. Cogging torque.

According to (21), the linear force F_{Fl} will only be influenced by the equivalent structure permeance $1/\Lambda_F$ and leakage flux permeance Λ_σ.

When the motor works in the position where the linear coil and center PMs are in line, we have

$$\frac{1}{\Lambda_{FL}} = \frac{1}{\Lambda_{FR}}. \tag{22}$$

By combining (18-b) and (22), $1/\Lambda_F$ can be expressed as

$$\frac{1}{\Lambda_F} = \frac{1}{2\Lambda_{FL}} = \frac{1}{2\Lambda_{FR}}. \tag{23}$$

By ignoring the leakage flux permeance Λ_σ, and substituting (23) into (21), we get the following linear force equation:

$$F_{Fl} = \frac{2H_c\mu_r\mu_0 N_L I_L L_r}{1 + \frac{\mu_r\mu_0 A_m}{h_m}(\frac{1}{2\Lambda_{FL}} + \frac{\delta_1}{\mu_0 A_{\delta 1}})}. \tag{24}$$

According to the torques in (16) and (24) for the basic and proposed models, respectively, it can be concluded that F_{Fl} will be smaller than F_l based on the high value of Λ_{FL} compared to Λ_L. Therefore, it is necessary to verify the forces of the basic and proposed models using the FEM to determine the exact difference. This is process is discussed in the next section.

IV. FEM ANALYSIS OF AN RL-SVCM

A. ROTARY MOTION ANALYSIS

Figure 13 presents the back electromotive force (EMF) of the basic and proposed models during one phase of rotary motion. One can see that the proposed model provides improvements compared to the basic model.

Additionally, Figure 14 presents the cogging torque values of rotary motion. The cogging torque of the proposed model is in the range of −0.8 to 0.8 N, whereas that of the basic model

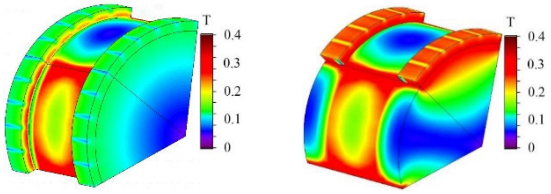

FIGURE 15. Rotor flux density distributions: (a) basic model and (b) proposed model.

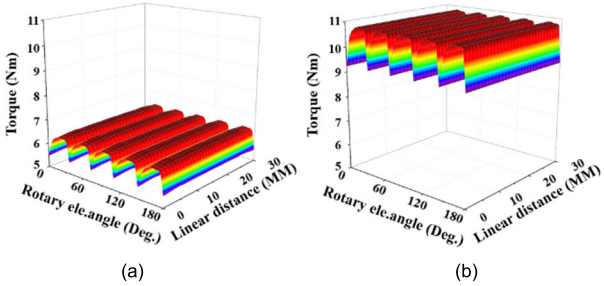

FIGURE 16. Rotary torque under rotary electrical angles *vs.* linear motion distances: (a) basic model and (b) proposed model.

lies in the range of −0.4 to 0.4 N. This is because the more PM volume in the proposed model compared to that in the basic model causes the more magnetic field energy [32], [34].

Figure 15(a) presents the rotor flux density distribution of the basic model with iron flux bridges under no load, where the flux density at the iron flux bridges is very small. This indicates that the iron flux bridges of the basic model are not involved in the generation of rotary torque. Figure 15(b) presents the rotor flux density distribution of the proposed model with PM flux bridges under no load. By comparing Figures 15(a) and 15(b), one can see that the flux density in the PM flux bridges of the proposed model is much greater than in the iron flux bridges of the basic model. This demonstrates that the PM flux bridge of the proposed model are involved in the generation of rotary torque.

Figures 16(a) and 16(b) present the rotary torque distributions of the basic and proposed models under rotary electrical angles versus linear motion distances. When the rotor is in the position where the linear coil and center PMs are in line, the rotary torque ripple of the basic model is 14.9% and that of the proposed model is 15.2%. Because the cogging torque of the proposed model is bigger than the basic model, the torque ripple of the proposed model has increased a little. The torque ripple increased 0.3% in the proposed model compared to the basic model.

In the simulation of the basic model and proposed model, the rotary coil current and the linear coil current are loaded at the same time. The operation of the motor will be affected by the coupling effect when the two kinds of current work together. To determine the coupling effect by checking if the average torque changes as the linear distance changes, we define the concept of ''torque fluctuation.'' Torque fluctuation is defined as the percentage difference between the maximum average torque and minimum average torque at

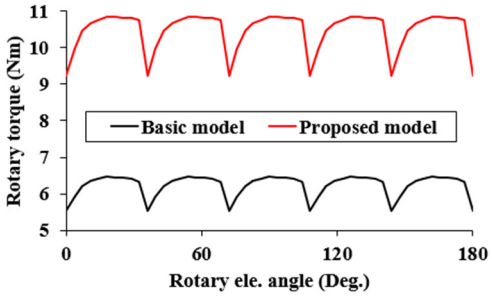

FIGURE 17. Rotary torque in the position where the linear coil and center PMs are in line.

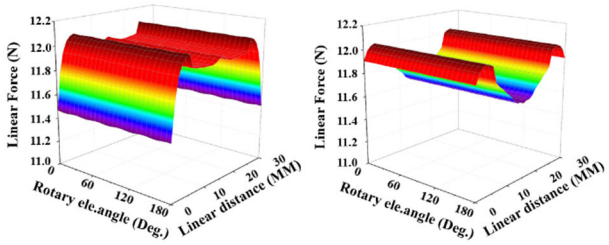

FIGURE 18. Linear force distribution under linear motion distances *vs.* rotary electrical angles: (a) basic model and (b) proposed model.

different linear distances. The basic model's torque fluctuation is 1% and the proposed model's torque fluctuation is 0.1%. Therefore, the rotary torque is virtually unaffected by the z-axis linear distance in both models. Also, the torque is less affected by the coupling effect in the proposed model compared to the basic model. Figure 17 presents a torque comparison of the two models in the position where the linear coil and center PMs are in line. When the rotor is in this position, the average torque of the basic model is 6.25 Nm and the average torque of the proposed model is 10.51 Nm. The torque of the proposed model is significantly greater than that of the basic model.

B. LINEAR MOTION ANALYSIS

Figures 18(a) and 18(b) present the linear force distributions of the basic and proposed models under linear motion distances versus rotary electrical angles. The force ripple of the basic model is 5.1% and the force ripple of the proposed model is 3.3%. This difference is caused by the influence of leakage flux. The force of the basic model decreases significantly at both ends compared to the proposed model. Therefore, the force ripple in the basic model is slightly greater than that in the proposed model.

Similar to torque fluctuation, ''linear force fluctuation'' is defined as the percentage difference between the maximum average linear force and minimum average linear force at different rotary electrical angles. The linear force fluctuation of the basic model is 0.03% and that of the proposed model is 0.01%. Therefore, the force distribution is not influenced by the rotary electrical angle in either model. Also, the linear force is less affected by the coupling effect in the proposed

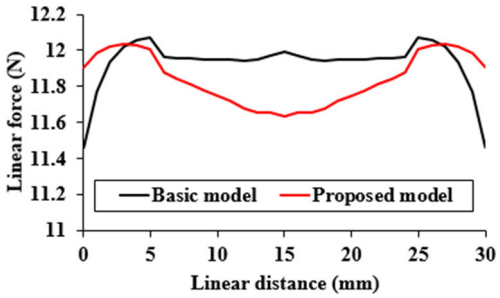

FIGURE 19. Linear force under no rotary motion.

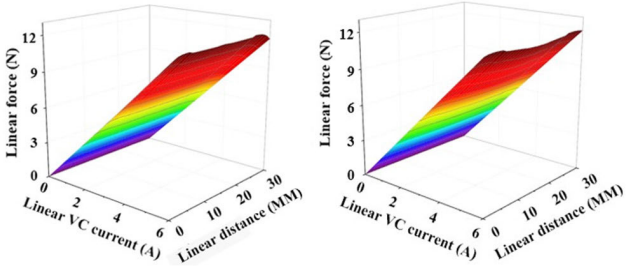

FIGURE 20. Linear force distributions under constant currents vs. axial linear distances: (a) basic model and (b) proposed model.

TABLE 3. FEM analysis results for machine performance.

	Basic Model	Proposed Model
Torque average	6.25 Nm	10.51 Nm
Torque ripple	14.9%	15.2%
Torque density	7391 Nm/m^3	12428 Nm/m^3
Force average	11.99 N	11.64 N
Force ripple	5.1%	3.3%
Force density	14179 N/m^3	13753 N/m^3

model compared to the basic model. The average force of the basic model is 11.99 N and the average force of the proposed model is 11.64 N. The force of proposed model is 2.9% lower than that of the basic model, which is consistent with the previous MEC analysis.

Figure 19 presents a linear force comparison between the two models under no rotary motion.

Figure 20 presents the linear force distributions of the basic and proposed models under constant currents versus axial linear distances. In these figures, the force changes almost linearly as the current increases. One can see that the change in force in the axial direction is not affected by the magnitude of the voice coil current.

Table 3 summarizes the performances of the two models. In this table, the rotary torque of the proposed model is 68.2% greater than that of the basic model. The torque density of the proposed model is also increased compared to the basic model. However, the linear force of the proposed model is 2.9% lower than that of the basic model.

V. PROTOTYPE MANUFACTURING AND EXPERIMENT

To verify the FEM analysis results, a prototype RL-SVCM with PM flux bridges was manufactured for experimental verification. Figure 22(a) presents the stator without the

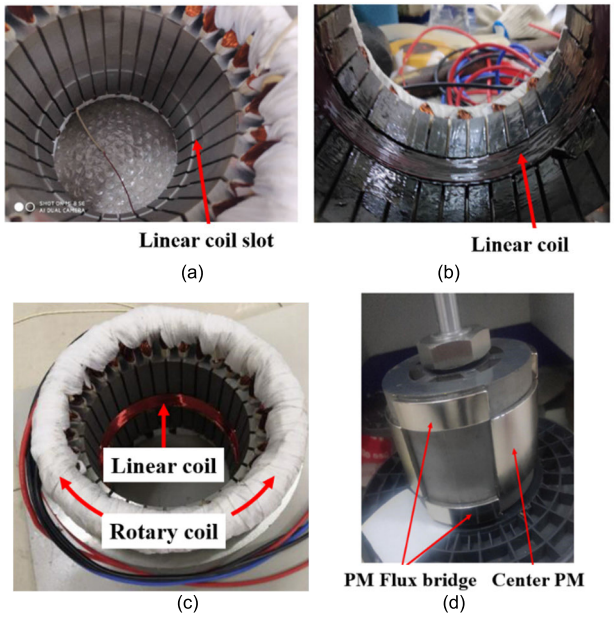

FIGURE 21. Manufactured prototype of the proposed model: (a) linear coil slot of the stator, (b) Linear coil embedded in the slot, (c) stator with linear and rotary coils, and (d) rotor with center PM and a PM flux bridge.

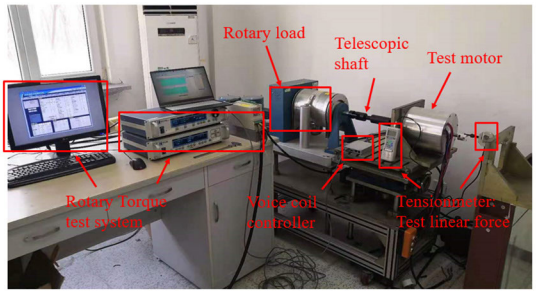

FIGURE 22. Experimental test setup.

linear coil, where one can clearly see the linear coil slot. Figure 22(b) presents the slot filled by the linear coil. Figure 22(c) presents the entire stator, where both the linear coil and rotary coil are clearly visible. Figure 22(d) presents the rotor, where one can see the center PM and a PM flux bridge.

Our experiment method was the same as our simulation method. The motor operated under rotary motion in the x-axis direction. During the experiment, both rotational motion current and linear motion current were applied.

The experimental setup is presented in Figure 22. In this experimental test system, there are two types of controllers. One controller controls rotary motion and the rotary torque can be checked by the rotary toque test system. The other voice coil controller controls linear motion. The linear force can be checked by the tension meter. By changing the x-axis positions, the linear force can be obtained.

A comparison of the FEM and experimental back EMF results is presented in Figure 23 at 50 rpm, rather than 1800 rpm, based on experimental limitations. The back EMFs of the FEM and experimental results match closely.

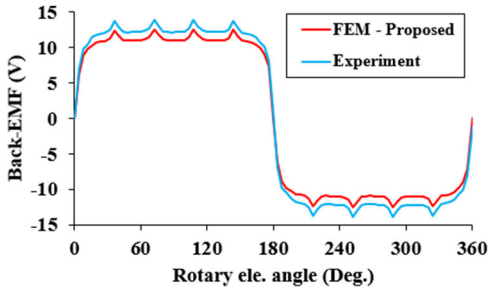

FIGURE 23. Back EMF values for the proposed model in the FEM and experimental results under no load.

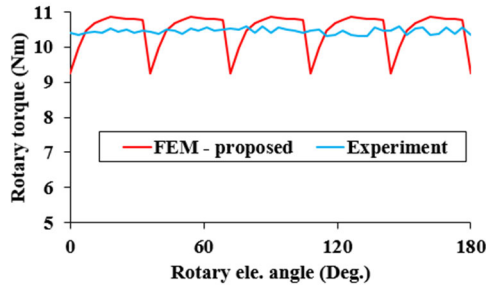

FIGURE 24. Rotary torque in the position where the linear coil and center PMs are in line.

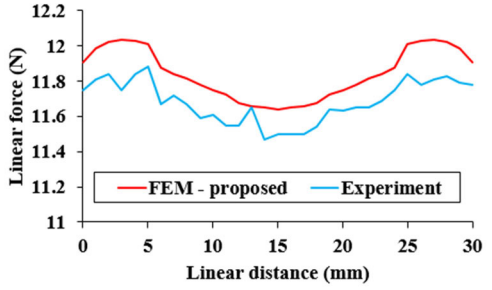

FIGURE 25. Linear force under linear motion distances alone from the FEM and experimental results.

TABLE 4. RL-SVCM with PM flux bridges: comparison of experimental and simulation results.

	Simulation	Experiment
Back EMF (V)	12.16	12.048
Rotary torque average (Nm)	10.51	10.48
Linear force average (N)	11.64	11.43

Figure 24 presents the FEM and experimental rotary torque values in the position where the linear coil and center PMs are in line. The average torque values of the FEM and experimental results are 10.51 Nm and 10.48 Nm, respectively. The torque ripple of the experiment result is much lower than that of the simulation result. It is mainly due to the inertia of the rotating mass that has tendency to smoothen the torque [35].

Figure 25 presents the linear force values under linear motion distances alone from the FEM and experimental results. The average torque values of the FEM and experimental results are 11.64 N and 11.43 N, respectively.

The FEM and experimental results for the proposed RL-SVCM with PM flux bridges are summarized in Table 4. One can see that the experimental results are largely consistent with the FEM results.

VI. CONCLUSION

This paper proposed an RL-SVCM with PM flux bridges for output performance improvement. The PM flux bridges can generate rotary torque, which can increase the overall rotary torque density. The iron flux bridges in the basic model cannot participate in rotary motion. The MEC method was used to explore the theoretical reasons for the improvements provided by the proposed model. The FEM was used to analyze the precise output performance of the proposed motor. To verify the FEM results, a prototype RL-SVCM with PM flux bridges was manufactured for experimental verification. Close agreement between the experimental results and the simulation results proves the feasibility of the proposed RL-SVCM.

REFERENCES

[1] Y. Zheng and J. Duan, "Materials and fabrication issues of micro V-groove for optoelectronics packaging," *Adv. Mater. Res.*, vols. 295–297, pp. 1330–1334, Jul. 2011.
[2] J. Lee and S. Wang, "Topological shape optimization of permanent magnet in voice coil motor using level set method," *IEEE Trans. Magn.*, vol. 48, no. 2, pp. 931–934, Feb. 2012.
[3] L. Xie, J. Si, Y. Hu, and Z. Wang, "Overview of 2-degree-of-freedom rotary-linear motors focusing on coupling effect," *IEEE Trans. Magn.*, vol. 55, no. 4, pp. 1–11, Apr. 2019.
[4] S. Tanaka, T. Shimono, and Y. Fujimoto, "Development of a cross-coupled 2DOF direct drive motor," in *Proc. IECON 40th Annu. Conf. IEEE Ind. Electron. Soc.*, Oct. 2014, pp. 508–513.
[5] M. Mori, W. Kitagawa, and T. Takeshita, "Characteristic analysis of 2-degree-of-freedom cylindrical actuator," in *Proc. 16th Int. Symp. Appl. Electromagn. Mech.*, vol. 45, nos. 1–4, pp. 257–264, 2014.
[6] J. Si, L. Xie, X. Xu, Y. Zhu, and W. Cao, "Static coupling effect of a two-degree-of-freedom direct drive induction motor," *IET Electr. Power Appl.*, vol. 11, no. 4, pp. 532–539, Apr. 2017.
[7] J. Si, L. Xie, J. Han, H. Feng, W. Cao, and Y. Hu, "Mathematical model of two-degree-of-freedom direct drive induction motor considering coupling effect," *J. Elect. Eng. Technol.*, vol. 12, no. 3, pp. 1227–1234, 2017.
[8] L. Xu, M. Lin, X. Fu, and N. Li, "Design and analysis of a double-stator linear–rotary permanent-magnet motor," *IEEE Trans. Appl. Supercond.*, vol. 26, no. 4, pp. 1–4, Jun. 2016.
[9] L. Xu, M. Lin, X. Fu, and N. Li, "Analysis of a double stator linear rotary permanent magnet motor with orthogonally arrayed permanent magnets," *IEEE Trans. Magn.*, vol. 52, no. 7, pp. 1–4, Jul. 2016.
[10] L. Xu, M. Lin, X. Fu, K. Liu, and B. Guo, "Analysis of the end-effects in double stator linear-rotary permanent magnet motor with long mover," in *Proc. CEFC*, Miami, FL, USA, Nov. 2016, p. 1.
[11] S. Fang, K. Guo, H. Lin, D. Wang, and H. Yang, "Electromagnetic analysis of a HTS linear-rotary permanent magnet actuator," *IEEE Trans. Appl. Supercond.*, vol. 26, no. 7, pp. 1–5, Oct. 2016.
[12] K. Guo, S. Fang, H. Lin, Y. Huang, Y. Zhang, and H. Yang, "A linear-rotary permanent magnet actuator with independent magnetic circuit structure," *IEEE Trans. Appl. Supercond.*, vol. 26, no. 7, pp. 1–6, Oct. 2016.
[13] M. M. Nezamabadi, E. Afjei, M. R. Naemi, and A. A. Afjei, "Design and 3D-FEM of a rotary-Linear switched reluctance motor," in *Proc. Int. Symp. Power Electron, Elect. Drives, Automat. Motion (SPEEDAM)*, Anacapri, Italy, Jun. 2016, pp. 430–434.
[14] M.-Z. Luo, H.-B. Zhou, J.-A. Duan, and B.-Q. Kou, "Design and analysis of a servo control system for a novel linear-rotary voice coil motor," in *Proc. 19th Int. Conf. Elect. Mach. Syst. (ICEMS)*, Chiba, Japan, Nov. 016, pp. 1–5.

[15] Z.-J. Zhang, H.-B. Zhou, J.-A. Duan, and B.-Q. Kou, "Design and analysis of two-degree-of-freedom voice coil motors for linear-rotary motion," in *Proc. 19th Int. Conf. Elect. Mach. Syst. (ICEMS)*, Chiba, Japan, Nov. 2016, pp. 1–6.

[16] F. Xing and B.-I. Kwon, "Design of a rotary-linear motor with unipolar SPM and voice coil structure," *IEEE Access*, vol. 8, pp. 150291–150300, 2020, doi: 10.1109/ACCESS.2020.3016646.

[17] Y.-D. Chen, C.-C. Fuh, and P.-C. Tung, "Application of voice coil motors in active dynamic vibration absorbers," *IEEE Trans. Magn.*, vol. 41, no. 3, pp. 1149–1154, Mar. 2005.

[18] H.-C. Yu, T.-Y. Lee, S.-J. Wang, M.-L. Lai, J.-J. Ju, D.-R. Huang, and S.-K. Lin, "Design of a voice coil motor used in the focusing system of a digital video camera," *IEEE Trans. Magn.*, vol. 41, no. 10, pp. 3979–3981, Oct. 2005.

[19] R. Banik and D.-G. Gweon, "Design and optimization of voice coil motor for application in active vibration isolation," *Sens. Actuators A, Phys.*, vol. 137, no. 2, pp. 236–243, Jul. 2007.

[20] Q. Chen, G. Xu, G. Liu, W. Zhao, L. Liu, and Z. Lin, "Torque ripple reduction in five-phase IPM motors by lowering interactional MMF," *IEEE Trans. Ind. Electron.*, vol. 65, no. 11, pp. 8520–8531, Nov. 2018.

[21] Q. Chen, G. Liu, W. Zhao, and G. Xu, "Separation and comparison of average torque in five-phase IPM machines with distributed and fractional slot concentrated windings," *IET Electr. Power Appl.*, vol. 13, no. 3, pp. 285–293, Mar. 2019.

[22] G. Liu, L. Liu, Q. Chen, and W. Zhao, "Torque calculation of five-phase interior permanent magnet machine using improved analytical method," *IEEE Trans. Energy Convers.*, vol. 34, no. 2, pp. 1023–1032, Jun. 2019.

[23] X. Liu, H. Chen, J. Zhao, and A. Belahcen, "Research on the performances and parameters of interior PMSM used for electric vehicles," *IEEE Trans. Ind. Electron.*, vol. 63, no. 6, pp. 3533–3545, Jun. 2016.

[24] Z. Zhang, C. Xia, H. Wang, and T. Shi, "Analytical field calculation and analysis of surface inset permanent magnet machines with high saliency ratio," *IEEE Trans. Magn.*, vol. 52, no. 12, pp. 1–12, Dec. 2016.

[25] M. Si, X. Yang, S. Zhao, and J. Si, "Development of the equivalent magnetic circuit model for a surface-interior permanent magnet synchronous motor," in *Proc. 6th Int. Conf. Power Electron. Syst. Appl. (PESA)*, Dec. 2015, pp. 1–4.

[26] J.-W. Jung, H.-I. Park, J.-P. Hong, and B.-H. Lee, "A novel approach for 2-D electromagnetic field analysis of surface mounted permanent magnet synchronous motor taking into account axial end leakage flux," *IEEE Trans. Magn.*, vol. 53, no. 11, pp. 1–4, Nov. 2017.

[27] A. Hemeida and P. Sergeant, "Analytical modeling of surface PMSM using a combined solution of Maxwell–s equations and magnetic equivalent circuit," *IEEE Trans. Magn.*, vol. 50, no. 12, pp. 1–13, Dec. 2014.

[28] B. Philips, "Techn review," vol. 35, no. 4, pp. 77–95, 1975.

[29] N. Bianchi and T. M. Jahns, *Design, Analysis, and Control of Interior PM Synchronous Machines*. Seattle, WA, USA: IEEE Industry Applications Society, Oct. 2004.

[30] T. A. Lipo, *Introduction to AC Machine Design*. Madison, WI, USA: Univ. Wisconsin-Madison, 2011, pp. 527–581.

[31] X. Sun, Z. Shi, G. Lei, Y. Guo, and J. Zhu, "Analysis and design optimization of a permanent magnet synchronous motor for a campus patrol electric vehicle," *IEEE Trans. Veh. Technol.*, vol. 68, no. 11, pp. 10535–10544, Nov. 2019.

[32] D. Wang, X. Wang, and S.-Y. Jung, "Cogging torque minimization and torque ripple suppression in surface-mounted permanent magnet synchronous machines using different magnet widths," *IEEE Trans. Magn.*, vol. 49, no. 5, pp. 2295–2298, May 2013, doi: 10.1109/TMAG.2013.2242454.

[33] Y. Pang, Z. Q. Zhu, and Z. J. Feng, "Cogging torque in cost-effective surface-mounted permanent-magnet machines," *IEEE Trans. Magn.*, vol. 47, no. 9, pp. 2269–2276, Sep. 2011, doi: 10.1109/TMAG.2011.2147326.

[34] D. Wang, H. Lin, H. Yang, Y. Zhang, and K. Wang, "Cogging torque optimization of flux memory pole-changing permanent magnet machine," *IEEE Trans. Appl. Supercond.*, vol. 26, no. 4, pp. 1–5, Jun. 2016, doi: 10.1109/TASC.2016.2535361.

[35] A. Zulu, B. C. Mecrow, and M. Armstrong, "A wound-field three phase flux-switching synchronous motor with all excitation sources on the stator," *IEEE Trans. Ind. Appl.*, vol. 46, no. 6, pp. 2363–2371, Jun. 2010.

FUZHEN XING was born in Liaoning, China, in 1991. He received the B.S. degree in electrical engineering from the Shenyang University of Technology, in 2014. He is currently pursuing the Ph.D. degree with the Department of Electronic Engineering, Hanyang University, South Korea. His research interest includes motor design and analysis.

JUNG-WOO KWON was born in 1992. He received the B.S. degree in bio-nano engineering and electrical engineering from Hanyang University, Ansan, South Korea, in 2015, and the M.S. and Ph.D. degrees from Hanyang University, in 2019. He currently holds a postdoctoral position with the Department of Electrical and Electronic Engineering, Hanyang University. His research interest includes electric machines, especially on motors.

MINGJIE LI was born in Hubei, China, in 1995. He received the B.S. degree in automation from the Chongqing University of Science and Technology, Chongqing, China, in 2016. He is currently pursuing the M.S. degree in electrical engineering with the Department of Electrical and Electronic Engineering, Hanyang University, Ansan, South Korea. His research interest includes the design, analysis, and modeling of electric machines.

BYUNG-IL KWON (Senior Member, IEEE) was born in 1956. He received the B.S. and M.S. degrees in electrical engineering from Hanyang University, Ansan, South Korea, in 1981 and 1983, respectively, and the Ph.D. degree in electrical engineering and machine analysis from The University of Tokyo, Tokyo, Japan, in 1989.

From 1989 to 2000, he was a Visiting Researcher with the Faculty of Science and Engineering Laboratory, Waseda University, Tokyo, Japan. In 1990, he was a Researcher with the Toshiba System Laboratory, Yokohama, Japan. In 1991, he was a Senior Researcher with the Institute of Machinery and Materials Magnetic Train Business, Daejeon, South Korea. From 2001 to 2008, he was a Visiting Professor with the University of Wisconsin–Madison, Madison, WI, USA. He is currently a Professor with Hanyang University. His research interest includes the design and control of electric machines.